

**Investigations of skeletal layer microstructure in the context of remote sensing of oil
in sea ice**

Authors: Zoe R. Courville¹, Ross Lieb-Lappen¹, Keran Claffey¹, Bruce Elder¹

¹US Army Corps of Engineers Engineering Research and Development Center Cold Regions Research and Engineering Laboratory, 72 Lyme Road, Hanover, NH 03755

ABSTRACT (2017-159)

The Arctic Oil Spill Response Technology – Joint Industry Program (JIP) funded a controlled basin experiment in November 2014 to assess the relative capabilities of a variety of oil in ice remote sensing techniques. An 80-cm sheet of level salt-water ice was grown in the Test Basin facility at the US Army Corps of Engineers Cold Regions Research and Engineering Laboratory (CRREL) in Hanover, New Hampshire. The basin ice was representative of natural level sea ice grown under quiescent conditions. This created a controlled baseline environment to compare different sensors with a manageable number of variables. The sensor testing spanned a two-month ice growth phase and a one-month decay/melt period. The detailed physical and electrical properties of the lab-grown ice sheet were monitored over the course of the experiment.

Analysis of preliminary sensor data revealed that the skeletal layer--the soft, porous band of new ice crystals at the growing ice water interface--plays a significant role in the process of incorporation of oil into the ice sheet, with oil infiltration occurring between the small lamellae structures. In addition, the underwater sensors, particularly

acoustic sensors, appeared to be very sensitive to skeletal layer properties, especially the surface roughness of the ice/water interface and the density of the skeletal layer.

Preliminary X-ray micro-computed tomography (micro-CT) data collected as part of the experiment demonstrated a qualitative scale dependence of sensor response to the skeletal layer microstructure. We used a cold-hardened Bruker SkyScan 1173 micro-CT scanner, housed in a -10 °C cold room, to generate full 3-dimensional x-ray images of the sea ice samples. We have demonstrated that the system is capable of distinguishing areas of void space, brine, ice, and oil at 40 micron resolution. The micro-CT scans were used to characterize the skeletal layer of the ice, including measuring density, thickness, orientation and spacing of the lamellae at 39 – 71 micron voxel resolution.

Characterizing the ice structure with high resolution micro-CT imaging may resolve some of the ambiguity in the sensor measurements and lead to improved accuracy of the numerical models that predict sensor performance in different oil and ice scenarios.

INTRODUCTION

The recent, retreat of Arctic sea ice in the summer period has resulted in a renewed interest in the exploitation of the Arctic for more direct shipping routes, access to fishing grounds, mineral exploration and extraction, oil and gas exploration and tourism opportunities. Remoteness and extreme environments makes operations challenging. Although still very small compared with other world shipping corridors, with the gradually increasing levels of vessel traffic related mostly to mining and tourism, comes the greater risks of a spill in Arctic waters.

2017 INTERNATIONAL OIL SPILL CONFERENCE

In January 2012, the international oil and gas industry launched a collaborative effort to enhance Arctic oil spill capabilities under the auspices of the International Association of Oil and Gas Producers (IOGP). This collaboration, called the Arctic Oil Spill Response Technology Joint Industry Programme (JIP) was designed to expand Arctic oil spill response capabilities. To address the objectives associated with remote sensing, one of six key areas of research identified for research, the JIP sponsored an evaluation of existing remote sensing technologies (Puestow et al., 2013, Wilkinson et al., 2013), followed by a large-scale laboratory experiment to test the capabilities of the most promising sensors.

As part of the initial phase of the experiment, it became increasingly apparent that certain small-scale physical characteristics of the ice impacted the performance of the sensors, particularly acoustic-based technologies. In particular, the effect of lamellae structures of the bottom skeletal ice, was of interest in modeling the behavior of the acoustic signals (Tang et al., 2015; Basset et al., 2016), as had been suggested by previous studies (Stanton et al., 1986; Wen, 1991; Williams et al., 1992) which found that the most attenuation within sea ice occurs within the skeletal layer because of this layer's high porosity and permeability.

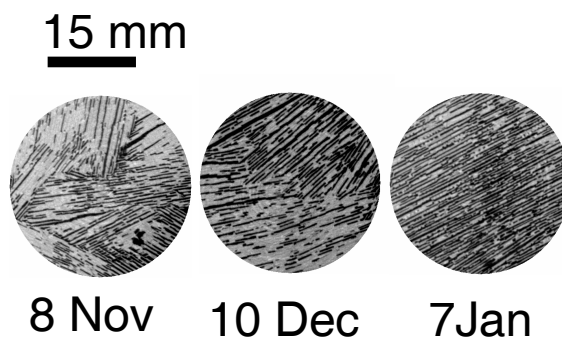


Figure 1. Lamellae structures as seen in cross-sections from micro-computed tomography imaging of cores. Grey is ice phase and black is air phase.

The microstructure of the skeletal layer is important in determining the entrainment of oil into sea ice structure (Petrich et al., 2013).

METHODS

1. Ice sheet construction and ice coring

Testing was conducted in the Test Basin facility at CRREL in Hanover, New Hampshire. Twenty tons of table salt (NaCl) were added to 250,000 gal of water in the tank to obtain a starting salinity of 25-27 ppt. Over a two-month period, an 80-centimeter thick sheet of level, salt-water ice was grown. During the growth phase the basin room temperature was near -24 °C. At predetermined ice thicknesses, Alaska North Slope crude oil at 0 °C was injected under the ice. After two months of growth phase, the basin air temperature was raised to near 0°C. To accelerate melt, the temperature was further raised to 5°C.

Ice core samples were drilled from the ice sheet nominally every 10 cm of increased thickness during the growth phase and prior to oil injection events. The core barrel was 7.5 cm in diameter. The hole was started by hand, and then a powered drill was used to drill through the remaining ice. Care was taken to prevent the drill from punching through the ice at the bottom of the ice sheet at the bottom of the core. Generally, three to four cores per coring session were retrieved for salinity, temperature, photographs, stratigraphy, thickness, micro-CT scanning, and thin and thick sectioning. In addition to core information, the air temperature, hole depth, freeboard, and water temperature and salinity were measured, along with information about the surface of the

ice where core sampling was conducted. Cores were sectioned such that the bottom 10-11 cm sample was first cut, and then placed right-side up in a container, suspended with the bottom of the core ~5 cm from the container bottom to allow brine to drain out of the sample. The bottom of the core was taken to the micro-CT facility immediately after drilling and cutting, and the outer diameter was shaved to ensure that the core had a diameter of 5 cm. The bottom of the core was scanned upside down to prevent destruction of the skeletal layer. The scans of the skeletal layer were started within 30 min of retrieval.

2. Micro-computed tomography methods

Samples of each ice core were scanned using a Bruker SkyScan 1173 desktop micro-CT scanner equipped with a Hamamatsu 130/300 tungsten X-ray source and a flat-panel sensor camera detector with 2240 x 2240 pixels. The SkyScan 1173 X-ray source produces a fixed conical, polychromatic beam with a spot size of $<5 \mu\text{m}$. We set the maximum accelerating voltage of the X-ray beam between 50 – 65 kV and a current between 123 – 130 μA . Samples were rotated 180° in $0.3 - 0.4^\circ$ steps, with 10-frame averaged attenuation images captured at each step using a camera exposure of 290 – 450 msec. We used a 2x2 binning protocol to create x-ray radiographs 1120x1120 pixels. The 10-cm cores were scanned as an oversized scan with 3 subsections, and complete scanning typically took 90 min to complete. We completed reconstruction of the resulting radiographs using Bruker SkyScan's NRECON software that uses a modified Feldkamp cone-beam algorithm to produce a vertical stack of gray-scale cross-section images. As part of image post-processing, we performed ring artifact reduction, post-alignment correction, beam hardening correction, and a two-pixel Gaussian kernel

smoothing to reduce noise. The resulting images had a spatial resolution of 39 – 71 μm per voxel and a 16-bit gray-scale dynamic range.

To analyze the skeletal layer, we selected a volume of interest (VOI) from the bottom of each ice core cropped vertically at the point where ice lamellae were no longer visible (17 mm – 56 mm in length). In the horizontal plane, we cropped the VOI to a smooth boundary at the ice core edge for each cross-sectional slice. Using a histogram shape-based approach, we set critical thresholds to segment the air/void phase from the ice/brine phase. We performed two-dimensional analysis on the resulting segmented cross-sectional images to calculate the structure thickness and separation of the ice phase as a measure of the lamellae thickness and separation over the depth of the skeletal layer per each cross-section of the micro-CT scan for every voxel of the reconstructed image. In three dimensions, the structure thickness of an object is computed by calculating the mean local thickness at given points within the solid. As defined by Hildebrand and Ruesegger (1997), the local thickness is the diameter of the largest sphere within the 3D structure that fulfils two conditions: 1) the sphere encloses the point (but the point is not necessarily the center of the sphere); and 2) the sphere is entirely bounded within the solid surfaces. In two dimensions, the structure thickness calculations use the assumption of the parallel plate model, where the thickness is assumed to be $2/(\text{surface to volume ratio})$ as described by Remy and Thiel (2002). The method starts with a “skeletonization” of the brine/ice phase, identifying the medial axes of all structures. The “sphere-fitting” local thickness measurement is made for all the voxels lying along the identified medial axis. The structure separation of the ice phase can be calculated as the structure thickness of the air phase.

Results/Discussion.

1. Skeletal layer evolution over time

Examples of the difference in the vertical structure of the skeletal layer of the ice during the two phases of the experiment, ice growth and melt out, are shown in Figure 2.

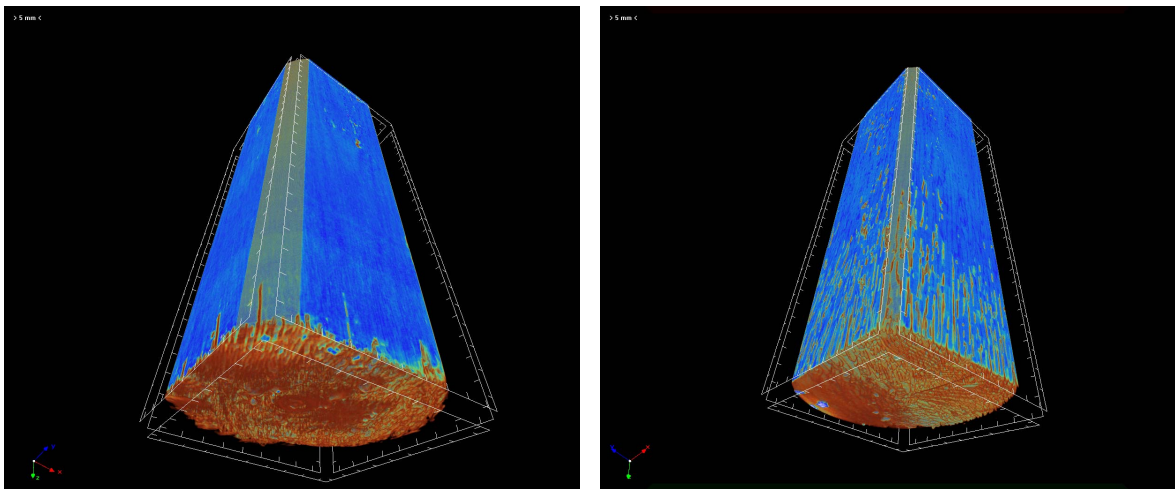


Figure 2. Three-dimensional images of the skeletal layer derived from micro-CT data showing the bottom of cores during ice growth phase (left) and during melt phase (right). Blue represents ice and red and orange represent air space. Tick marks are 5 mm in length.

As shown in Figure 3, the thickness of the skeletal layer was tracked versus time over the course of the experiment based on visual examination of the micro-CT images. The thickness of the layer stayed relatively constant during the first month of the experiment, and increased dramatically during the melt out phase, which started 13 Jan 2015. By the end of the experiment, the skeletal layer thickness had increased to 3 cm from the initial thickness of 1 cm.

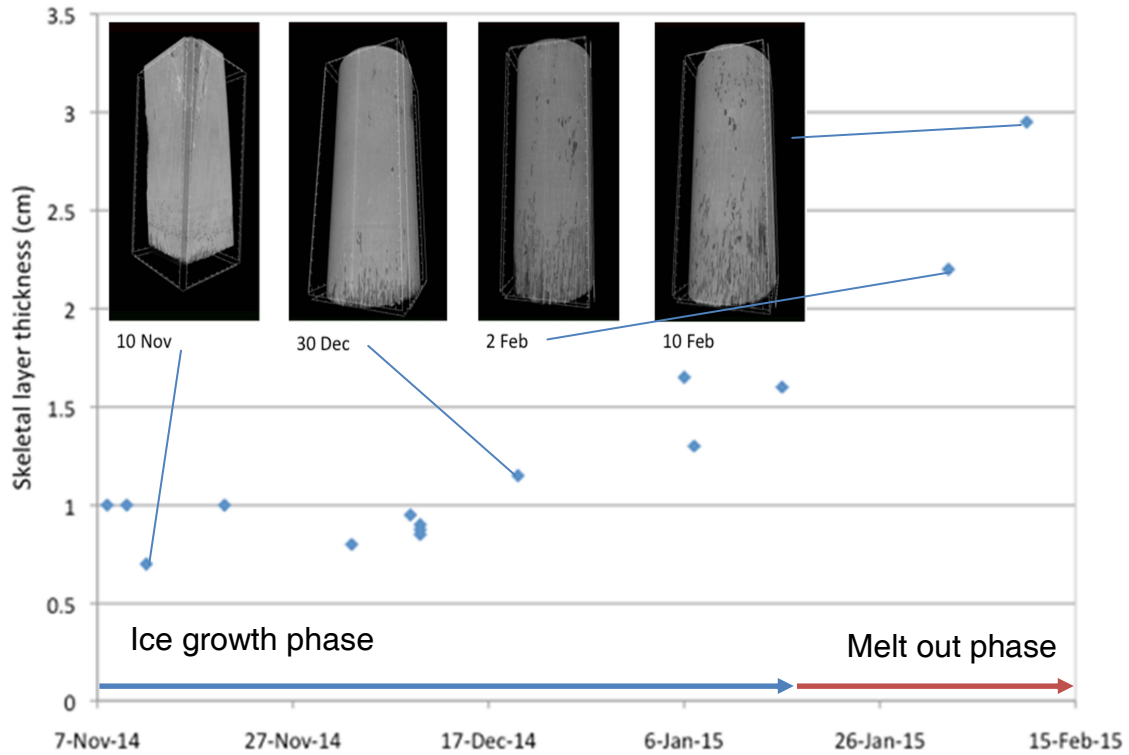


Figure 3. Evolution of skeletal layer thickness over time shown for ice growth (4Nov2015 to 12Jan2015) and melt out phase, which began 12Jan15, of experiment, with examples of micro-CT reconstructed 3D images from both phases (inset) showing general evolution over time. Blue lines indicate thickness measurement obtained from the corresponding micro-CT image.

2. Spatial variation of skeletal layer

In order to examine the meter-scale spatial variability of the skeletal layers, a series of cores was scanned on 10 Dec centered on a single point (see Figure 4 for location of cores). The skeletal layer was scanned to examine variations in skeletal layer thickness, lamellae structure, and lamellae spacing. Figure 5 shows the micro-CT data for 3 of the cores.

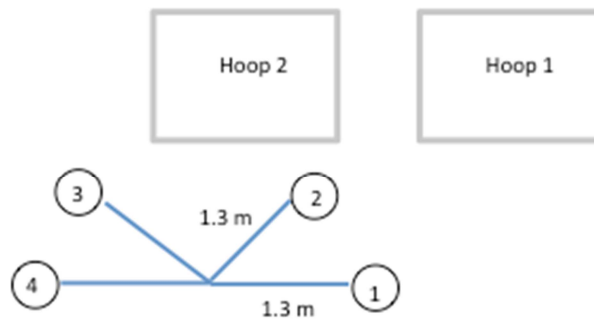


Figure 4. Schematic of core locations taken from 1.3m radii around acoustic sensor. Numbers correspond to core locations.

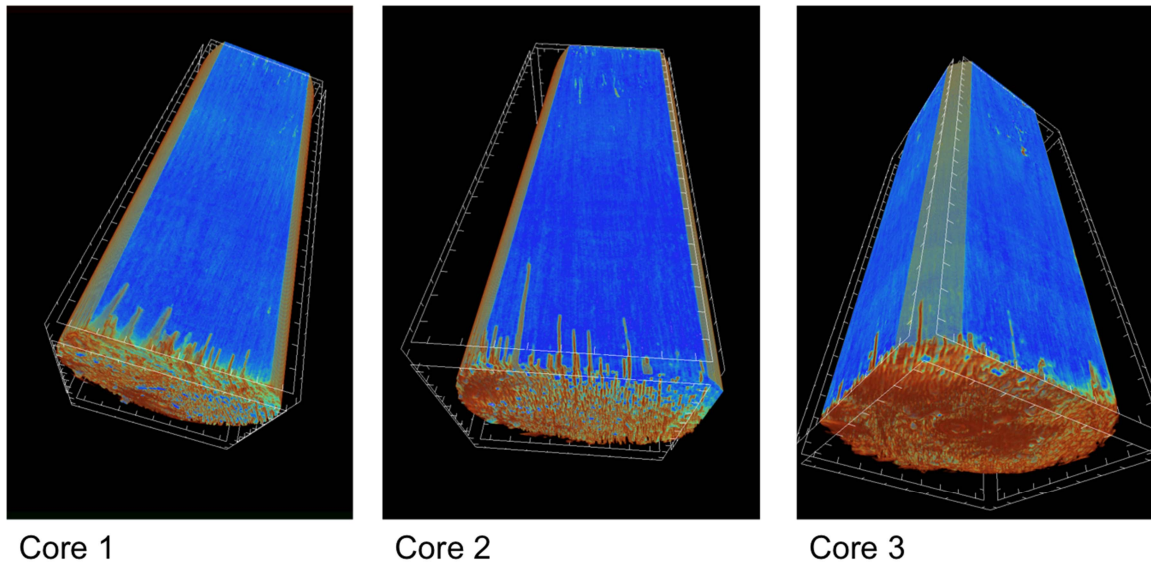


Figure 5. Variations in skeletal layer on meter-scale from 9Dec. Tick marks equal 5 mm in length. Dimensions of sections shown here are 4 cm in diameter, 11 cm in length.

The variation in skeletal layer thickness between individual cores spaced at ~1m+ intervals around the acoustic sensor is nearly equivalent to the variation in thickness that occurs within the 4 cm-diameter footprint of the core samples. Skeletal layer thickness varies from 1-2 cm. In Core 1, average thickness is 1 cm. Core 2 has an average thickness of 1.5 cm, and Core 3 has an average thickness <1cm.

3. Lamellae evolution over time

The evolution of the lamellae structures within the skeletal layer as demonstrated by horizontal cross sections of the bottom of the core is shown in Figure 6. The lamellae structures became more rounded during the melt out phase and thicker after the initial growth phase.

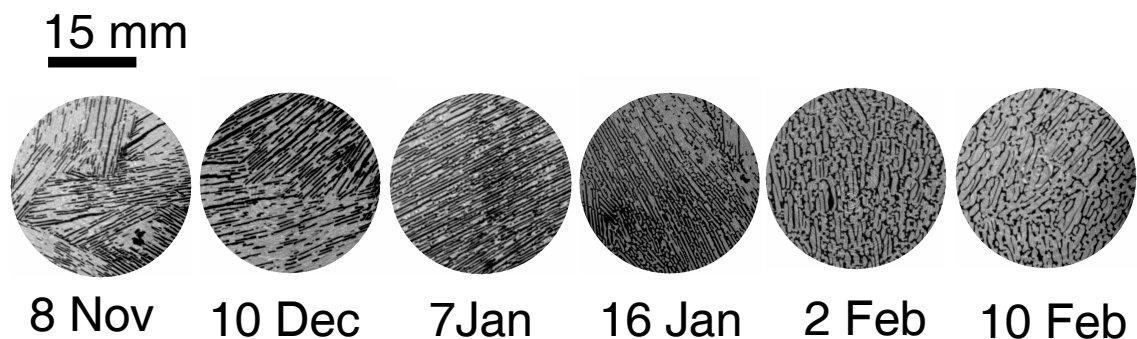


Figure 6. Evolution of lamellae structures over time. Grey is ice phase and black is air phase. Lamellae structures become generally thicker and more rounded during the melt out phase. Orientation of growth can be seen clearly in these images from 8 Nov to 10 Dec, when the diameter of individual crystals become larger than the region of interest shown in these images (~30 mm).

The thickness profile of the lamellae structures within the skeletal layer, as determined by calculating the mean structure thickness per cross-section, is shown as a function of depth in Figure 7.

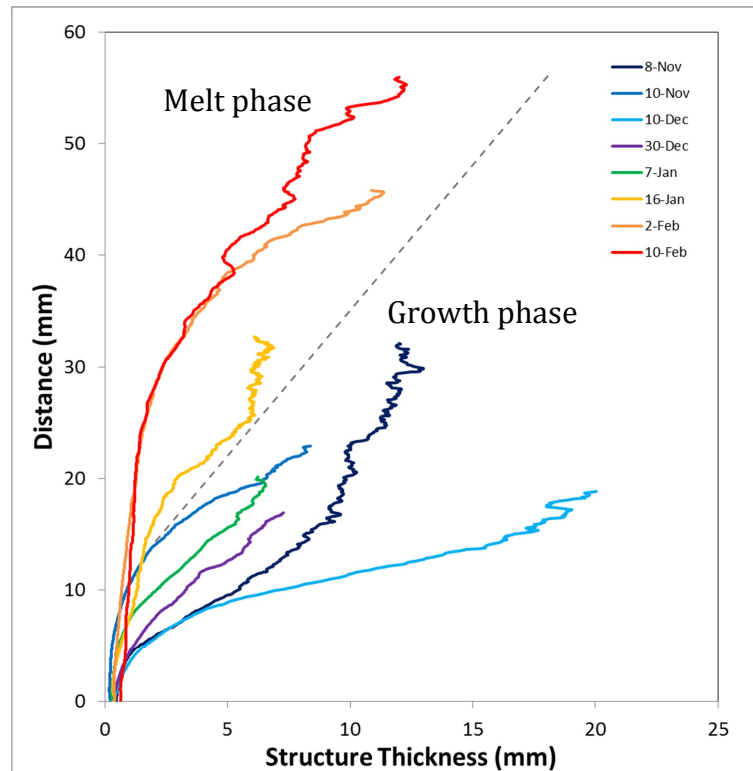


Figure 7. Lamellae thickness, as represented by the calculated mean structure thickness per 2D cross-section, along the skeletal layer of the cores. Blue/green colors are from the growth phase, while red/orange colors represent cores from the melt out phase. Dashed line indicates general boundary between growth and melt phases; melt started 12 Jan. Distance is measured from the bottom of the core.

Lamellae thickness profiles show that the thickness of the lamellae structures decreases with depth, until very thin structures with submillimeter thickness exist near the ice/water interface. The observed trend is consistent with existing sea ice growth theory and observations since ice lamellae grow vertically downward with initial spacing of 0.5 – 1 mm (Weeks and Ackley, 1986; Petrich and Eiken, 2010) at the bottom of the

ice sheet. These observations are also consistent with Anderson and Weeks (1958) observations of photographs of lamellae structures in warm ice (i.e. -20°C ice) with an average thickness of 0.46 mm; as well as consistent with Lofgren and Weeks (1969) laboratory observations for intermediate growth rates at low water salinity. Ice lamellae join and consolidate into sea ice at the boundary of the skeletal layer and the bulk of the ice. During this consolidation process, brine is expelled from the ice as described in detail by Petrich and Eiken (2010). As the sea ice continues to grow, the brine between lamellae cools and continues to freeze, rejecting the salts into narrower and narrower brine channels in the bulk of the ice.

The initial total vertical thickness of the skeletal layer on 8 Nov was approximately 3 cm (as indicated by corresponding line in Figure 7). During the growth phase, the total skeletal layer vertical thickness was approximately 2 cm. During the melt phase, 16 Jan to 10 Feb, the brine channels and the vertical extent of the skeletal layer thicken as the spacing between the lamellae at ice-sea water interface increases from 3.2 mm at the start of the melt phase to 5.6 mm at the end of the melt phase.

The thickness of the individual lamellae structures for the bottom 1 cm of the ice sheet is shown in Figure 8. The initial growth phase has thick lamellae structures, 0.47 mm thick, which then become thinner during the remainder of the growth phase to a relatively constant 0.2 -0.35 mm thick structure. During the melt phase, the lamellae structures become thicker from 0.36 mm at the start of the melt phase to 0.66 mm at the end of the melt phase.

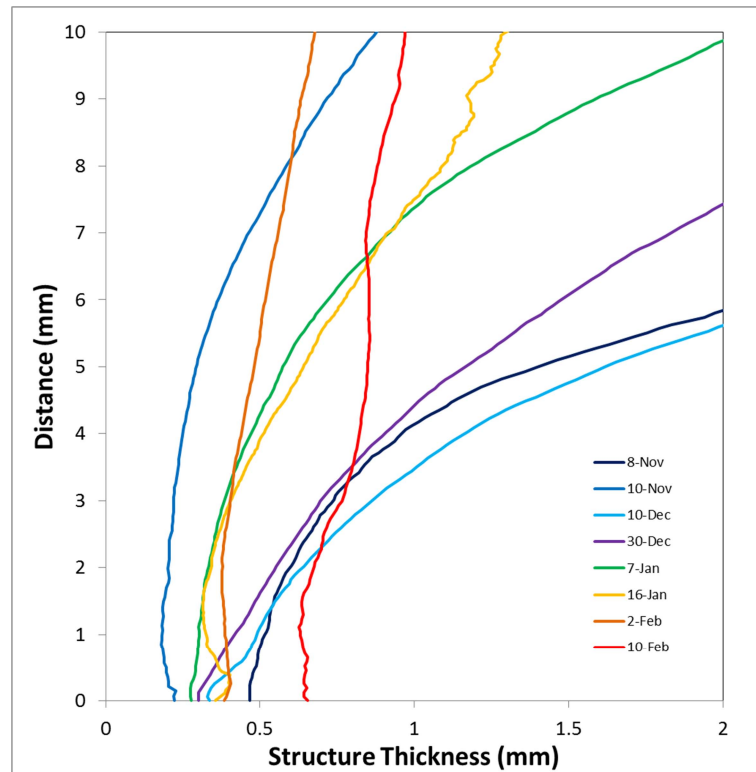


Figure 8. Lamellae thickness, as calculated from structure thickness, for the bottom 1 cm of the skeletal layer (enlargement of Figure 7). Blue/green colors are from the growth phase, while red/orange colors represent cores from the melt out phase; melt started 12 Jan. Distance of zero represents the bottom of the core.

The spacing between individual lamellae structures is calculated in a similar manner by using the air phase to calculate structure thickness of the air phase, or equivalently, structure separation of the ice/brine phase. This lamellae spacing is shown for the entirety of the skeletal layer thickness in Figure 9, and for the bottom 1 cm of the ice sheet in Figure 10. The spacing between lamellae increases with depth towards the bottom of the core, increasing rapidly towards the very bottom 1 cm.

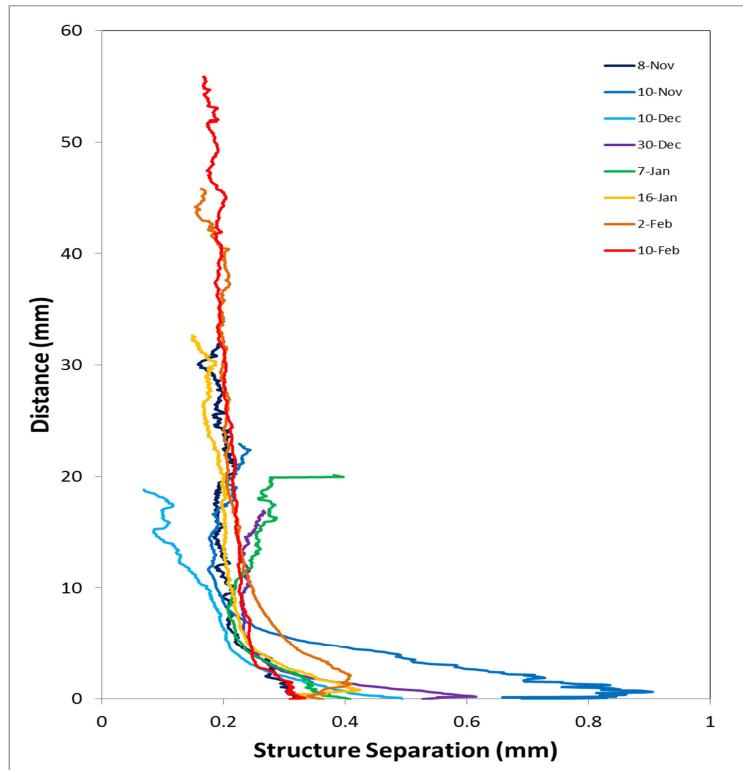


Figure 9. Lamellae spacing, as calculated from structure separation, throughout the thickness of the skeletal layer. Blue/green colors are from the growth phase, while red/orange colors represent cores from the melt out phase, which started 12 Jan. Distance of zero represents the bottom of the core.

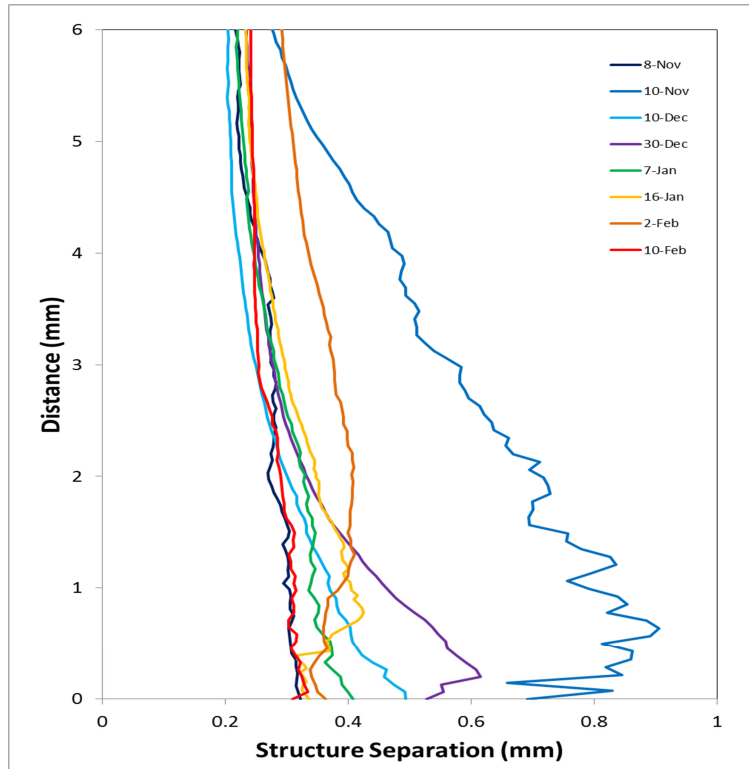


Figure 10. Lamellae spacing, as calculated from structure separation, for the bottom 1 cm of the skeletal layer (enlargement of Figure 9). Blue/green colors are from the growth phase, while red/orange colors represent cores from the melt out phase. Distance of zero represents the bottom of the core.

Spacing between the lamellae is initially 0.36 mm at the start of the growth phase on 8 Nov, and then rapidly increases to 0.69 on 10 Nov, after which the spacing decreases over time. During the melt out phase, spacing between the lamellae stays relatively constant from 0.31 mm to 0.36 mm. The observations of lamellae spacing are also consistent with previous observations of Anderson and Weeks (1969) of 0.23 mm with larger variations than lamellae thickness measurements in warm ice.

Conclusions.

The evolution of the structure of the skeletal layer of an artificially grown ice sheet has been described at high spatial resolution using a micro-CT scanner. The thickness of the skeletal layer can be described through the visual examination of the skeletal layer in the 3D reconstructions of the skeletal layer, and more quantitatively by the examination of the lamellae structures within the skeletal layer.

Close examination of the lamellae structures of the skeletal layer shows that the initial growth phase on 8 Nov had a relatively vertically thick, 3 cm, skeletal layer with 0.47 mm thick lamellae closely spaced apart at 0.33 mm. Lamellae separation increased with depth, contrary to the findings of Nakawo and Sinha, 1984, who found a rapid decrease in spacing towards the bottom of the core of natural sea ice at Eclipse Sound. During the subsequent growth phase, the skeletal layer remained at a relatively constant 2 cm average thickness with 0.2-0.35 mm thick lamellae spaced 0.4-0.7 mm apart. During melt, the skeletal layer grew from 3.2 cm thick to 5.6 mm thick with 0.4 to 0.66 mm thick lamellae spaced 0.3 to 0.4 mm apart.

The structure of the skeletal layer has important implications for the acoustic response of underwater remote sensing instruments. Incorporation of more realistic physical construction of the skeletal layer has the potential to improve the modeling of high frequency acoustic response through the incorporation of a thin skeletal layer with rough interfaces at the boundaries, i.e. Tang et al. (2015) and Basset et al. (2016).

ACKNOWLEDGEMENTS Funding for this research was provided by The Arctic Oil Spill Response Technology – Joint Industry Program (JIP). The authors wish to thank Leonard Zabilansky who oversaw the technical portions of the laboratory experiment at

CRREL, along with CRREL staff members Nate Lamie, Bill Burch, Jesse Stanley, Troy Arnold, Ben Winn, and Charlie Schelewa for providing invaluable assistance with all portions of the project.

REFERENCES

Anderson, D.L., and W.F. Weeks (1958) A theoretical analysis of sea ice strength, *EOS, Trans. AGU*, 39(4).

Basset, C., A.C. Lavery, T. Maksym, and J.P. Wilkinson (2016) Broadband acoustic backscatter from crude oil under laboratory-grown sea ice. *J. Acoust. Soc. Am.* 140(4) doi: 10.1121/1.4963876.

Hildebrand, T., and P. Ruegsegger (1997) A new method for the model independent assessment of thickness in three dimensional images. *J. Microsc.* **185**: 67-75.

Lofgren, G., and W.F. Weeks (1969) Effect of growth parameters on substructure spacing in NaCl ice crystals, *J. Geophys. Res.*, 74:52.

Nakawo, M., and N.K. Sinha (1984) A note on brine layer spacing of first-year sea ice, *Atmosphere-Ocean*, 22:2, 193-206, doi: 10.1080/07055900.1984.9649193.

Petrich, C., and H. Eicken (2010) Growth, structure and properties of sea ice. In *Sea Ice*, 2nd ed.; D.N. Thomas, G.S. Dieckmann, eds.; Wiley-Blackwell: Oxford, UK, pp. 247-282.

Petreich, C., J. Karlsson, and H. Eicken (2013) Porosity of growing sea ice and potential for oil entrainment, *Cold Reg. Sci. Tech.*, 87, 27-32.

Puestow, T., L. Parsons, I. Zakharov, N. Cater, P. Bobby, M. Fuglem, G. Parr, A. Jayasiri, S. Warren, and G. Warbanski (2013) Oil spill detection in low visibility and ice: surface remote sensing, *Final Report 5.1*, Joint Industry Programme to define the state-of-the-art for surface remote sensing technologies to monitor oil under varying conditions of ice and visibility, London, U.K. 82 pp.

Remy, E., and E. Thiel (2002) Medial axis for chamfer distances: computing look-up tables and neighbourhoods in 2D or 3D. *Pattern Recognition Letters* **23**: 649–661.

Stanton, T. K., P.H. Wiebe, D. Chu, and L. Goodman (1994) Acoustic characterization and discrimination of marine zooplankton and turbulence, *ICES J. Mar. Sci.* 51, 469–479.

Tang, D., D.R. Jackson, C. Bassett, and A. C. Lavery (2015) Modeling high-frequency acoustic backscatter for remote sensing of oil under sea ice and oil encapsulated in sea ice, *J. Acoust. Soc. Am.*, 138, 1744 doi:10.1121/1.4933499.

Weeks, W.F., and S.F. Ackley (1986) The growth, structure and properties of sea ice. In: *The Geophysics of Sea Ice*, N. Untersteiner, pp. 9-164, Plenum Press, New York (NATO ASI B146).

Wen, T., G.R. Garrison, R.E. Francois, R.P. Stein, and W.J. Felton, (1991) Sound speed, reflectivity, and absorption measurements in arctic ice in 1988, *Technical Report, Appl. Phys. Lab. Rep. APL-UW TR 9005*.

Wilkinson, J., T. Maksym, and H. Singh (2013) Capabilities for detection of oil spill under sea ice from autonomous underwater vehicles, *Final Report 5.2*, Joint Industry Programme on oil spill detection and mapping in low visibility and ice: focus on undersea remote sensing, London, U.K. 104 pp.

Williams, K. L., G.R. Garrison, and P.D. Mourad (1992) Experiment examination of growing and newly submerged sea ice including acoustic probing of the skeletal layer," *J. Acoust. Soc. Am.* 92(4), 2075–2092.